

2021-10

Compact floating wave energy converter arrays: Inter-device mooring connectivity and performance

Howey, B

<http://hdl.handle.net/10026.1/18212>

10.1016/j.apor.2021.102820

Applied Ocean Research

Elsevier

All content in PEARL is protected by copyright law. Author manuscripts are made available in accordance with publisher policies. Please cite only the published version using the details provided on the item record or document. In the absence of an open licence (e.g. Creative Commons), permissions for further reuse of content should be sought from the publisher or author.



Compact floating wave energy converter arrays: Inter-device mooring connectivity and performance

Ben Howey^a, Keri M. Collins^a, Martyn Hann^a, Gregorio Iglesias^b, Rui P.F. Gomes^c, João C. C. Henriques^c, Luís M.C. Gato^c, Deborah Greaves^{a,*}

^a School of Engineering, Computing and Mathematics, University of Plymouth, UK

^b School of Engineering and Architecture & MaREI, Environmental Research Institute, University College Cork, Ireland (formerly at the University of Plymouth)

^c IDMEC, LAETA, Instituto Superior Técnico, Universidade de Lisboa, Portugal

ARTICLE INFO

Keywords:

Wave energy
Interconnected moorings
Shared moorings and anchors
Offshore renewable energy
Ocean energy
Oscillating water column

ABSTRACT

Achieving cost reduction in wave energy conversion is seen as essential to enabling the progress of the sector. At utility scale in a wave farm, multiple devices are likely to be deployed in array configurations. Closely spaced, compact wave energy converter (WEC) arrays are a promising option for cost reduction, realising synergies in operation and maintenance tasks and auxiliary installations, whilst achieving economies of scale. Mooring and anchorage systems are known to be a major component of the structural costs, and the use of interconnecting lines between neighbouring devices can reduce the number of anchors and minimise total line length. In this paper, we present the experimental study of different configurations of a five-device array of spar-buoy oscillating-water-column wave energy converters in a wave basin, focusing on the analysis of the power production performance. The study compares the performance of a single isolated device, an array with independently-moored devices and three arrays with inter-body connections, with different levels of connectivity in the mooring arrangement. Results show considerable performance implications linked to the interconnecting of devices, with the interconnected array configurations yielding a 75% increase in the annual energy extracted compared to the baseline (non-interconnected) arrangement. The performance enhancements are primarily attributed to the interconnecting moorings resulting in greater heave motion at higher frequencies for which the phase relationship between the water column and heave motion is more beneficial. Evidence is also presented that positive intra-array effects occur within interconnected arrays when the wavelength is equal to the array spacing.

1. Introduction

Ocean waves represent a significant renewable energy resource, and global resources have been estimated to exceed 2 TW within a 30 nautical mile zone of non-polar land masses (Gunn and Stock-Williams, 2012). It is expected that if the energy in the waves is fully harnessed, this could satisfy the annual electricity generation of the world (26,700 TWh in 2018 International Energy Agency, 2020). A study for the Pacific Northwest region found that the wave resource is generally greater during winter months, when demand is higher, and is more predictable than wind or solar energy (Reikard et al., 2015). However, regardless of this potential, the wave energy industry has yet to develop past the point of full-scale technology demonstration deployments.

A significant issue for the developers of wave energy converters

(WECs) is the cost of such systems compared to other energy sources, both renewable and non-renewable. Estimates for the Levelised Cost of Energy (LCOE) of wave energy vary depending on multiple-factors, including the technology type and deployment location (Chang et al., 2018). For three reference wave energy converters, Jenne et al. (2015) found the average to be USD 4.25/kWh for a single WEC. This compares poorly to LCOE costs for offshore wind projects, which were approximated at USD 0.17/kWh (Wiser et al., 2016), with a target of under USD 0.13/kWh by 2020 (Brown et al., 2015), and have since seen further dramatic cost reduction in Europe (Jin and Greaves, 2021).

These figures indicate the need for a reduction in LCOE of wave energy and whereas cost reduction has been achieved in offshore wind through increasing the size of the turbine, point absorber type wave energy devices will need to be deployed in very large arrays (Folley,

* Corresponding author.

E-mail address: deborah.greaves@plymouth.ac.uk (D. Greaves).

<https://doi.org/10.1016/j.apor.2021.102820>

Received 22 February 2021; Received in revised form 30 April 2021; Accepted 24 July 2021

Available online 3 August 2021

0141-1187/© 2021 The Authors. Published by Elsevier Ltd. This is an open access article under the CC BY license (<http://creativecommons.org/licenses/by/4.0/>).

2016). Jenne et al. (2015) predicted that the USD 4.25/kWh average for a WEC could be reduced to USD 0.93/kWh for a 50-device array and USD 0.83/kWh for a 100-device array. Cost savings are expected for arrays as a result of the potential to share electrical cables and infrastructure as well as operation and maintenance costs. There is also the possibility for power captured by individual devices to be positively impacted by intra-array hydrodynamic interactions between devices. These intra-array interactions have been the focus of significant previous numerical studies, as reviewed by (Folley, 2016).

While few experimental studies into intra-array interactions have been conducted, Weller et al. (2010) studied experimentally an array of heaving wave energy devices supported by a fixed platform and found that although positive array interactions occurred in regular waves, these positive array effects were largely dependant on the incident wave period and the performance of adjacent devices. Stratigaki et al. (2014) carried out experiments on 25 heaving point absorber WECs supported on fixed structures in a range of geometric layouts, studying the impact on the wave field down-wave of the array. For a 5×5 array, a wave field attenuation of up to 18.1% and 20.8% was found in the lee of both linear and staggered configurations, respectively. The wave field alterations within the array were found to be highly dependant upon the array geometric layout, WEC spacing and the number of WECs. Ruiz, Ferri and Kofoed Ruiz et al. (2017) conducted measurements on an array of 5 devices to provide data for validation of a linearized potential flow theory array hydrodynamics tool. O'Boyle et al., (2017) conducted an experimental campaign to map, at high resolution, the wave field variation around arrays of 5 oscillating water column WECs.

In the aforementioned studies, devices within arrays have been either moored individually or arranged to oscillate independently relative to a common reference structure and so any intra-array effects are due to the hydrodynamic interactions between devices only and do not take into account any mooring interconnections. The mooring systems for arrays of individually moored devices have been estimated to make up 20–30% of the total structural costs (Thomsen et al., 2018). Therefore, a potential method to reduce array costs is to decrease the length of mooring line and number of anchors needed by interconnecting some of the devices within the array directly, without the anchoring to the seabed. Krivtsov and Linfoot (2014) conducted 1:20 scale experiments on closely-packed arrays of 3 and 5 floating Oscillating Water Columns (OWC) devices moored with shared anchors. Devices within the array were found to capture approximately 6% more energy than an individually deployed device (Ashton et al., 2009). However, it was found that for certain sea states the peak mooring loads in WEC arrays can be considerably higher than for an individual device. Correia da Fonseca et al. (2016) carried out an experimental campaign, studying an array of three interconnected spar buoy floating OWC WECs and found comparable power performance between the array and isolated device scenarios. Vicente et al. (2009) conducted a numerical study of an array of three point absorbers, each with one seabed line and one line connected to a central clump weight. Total array power capture was found to increase compared with the same number of individual devices across a frequency band, which was partially dependant on wave direction. Shared anchor systems for arrays of multi-body point absorbers were considered as part of an LCOE study Yang et al., 2018 comparing four array configurations. It was concluded that LCOE is sensitive to the hydrodynamic interaction between WECs and the mechanical couplings in the mooring design.

This paper reports on a series of physical laboratory-scale experiments designed to investigate the influence of mooring interconnectivity on the power capture performance of an array of floating WECs. The Instituto Superior Técnico (IST) Spar-buoy OWC-type WEC was used (Gomes et al., 2012). Results are reported from an individual device, an array of 5 WECs in die formation individually moored and in three interconnected configurations with varying degrees of interconnection. This approach has allowed for the impact of hydrodynamic intra-array interactions and the impact of interconnecting to be separately

identified. Section 2 details the different array configurations and the experimental methodology. In Section 3, the experimental results are discussed, and conclusions are presented in Section 4.

2. Experimental methodology

2.1. Array configuration and experimental layout

The Spar-buoy used for the interconnected array interaction study presented here is shown in Fig. 1 and is a floating OWC with a central water column through the length of the model and open at its base. The configuration used was a slight adaption of the Spar-buoy reported by da Fonseca et al. Correia da Fonseca et al., 2016, and an orifice plate is used to represent the power take-off (PTO) at model scale.

Experiments were conducted in the University of Plymouth's COAST laboratory Ocean Basin, which is a 35.5 m x 15.5 m basin with a raisable floor that can allow testing at different water depths up to a maximum of 3 m. Tests were conducted at a scale of 1:40 and a water depth of 2 m to represent the water depth (80 m) of the deployment site off the coast of Leixões, Portugal. Wave generation is achieved through 24 hinged flap-type paddles controlled by an Edinburgh Designs Ltd control system. The system is capable of creating regular, irregular and directional sea states with wave heights of up to 0.9 m at 0.4 Hz. Waves are absorbed at the opposite end to the paddles via a convex beach profile and the paddles also minimize reflections through a force feedback system. Details of the performance of the basin and beach system are given by (Collins et al., 2018).

A square array configuration of five devices was modelled in a die arrangement, with four devices located on the outer corners of the square and the fifth device at the centre. This configuration was selected as it provides a means to change the level of interconnectivity between devices systematically and allows sufficient space within the basin for the required mooring spread. It is also a modular configuration to which additional devices could be easily added in future deployments. The spacing of the five devices (TM1–5) and their location within the basin are given in Fig. 2, where a plan view of the COAST laboratory Ocean Basin and experiment layout is shown. Experiments were carried out with a water depth of 2.0 m. Data from two wave gauges (WG1 and WG2) were recorded in the basin during both wave-only tests and when the array was installed. These were located on the centreline of the basin, at positions 4.73 m for WG1 and 1.43 m for WG2 up-wave of the central device and shown in Fig. 2.

Five different configurations were tested in the experiments: a single isolated device (Configuration I), the five-device array of individually moored devices without interconnection (Configuration A) and three configurations of the five-device array with different levels of inter-body connection (Configurations B, C and D). The layout of the five-device array in die arrangement and its orientation to the wave generation system and tank walls is shown in Fig. 2, and in Fig. 3 the schematic arrangement of each configuration is illustrated. Configuration I is the central device of the array installed in isolation using a 3-point mooring comprising three bottom-mooring lines (BML) and provides a baseline from which array interaction effects may be assessed. The four outer devices were installed in addition to the central device to form the five-device array in a die arrangement (Fig. 2). In Configuration A, each device is individually moored in a similar way to the central device with three BMLs. In Configuration B, one BML is removed from each of the outer devices and replaced with an inter-body line connection to the central device (IBL1) and to its nearest neighbours (IBL2). In the interconnected configurations, the central device is no longer directly moored to the sea bed, while the outer devices have two bottom mooring lines each. In Configuration C, the number of BMLs is reduced to one for each outer device, and in Configuration D, inter-body lines (IBL2) between the four outer devices are also removed. The configurations in Fig. 3 were selected to allow both the hydrodynamic array effects and the impact of different levels of interconnection between devices in the

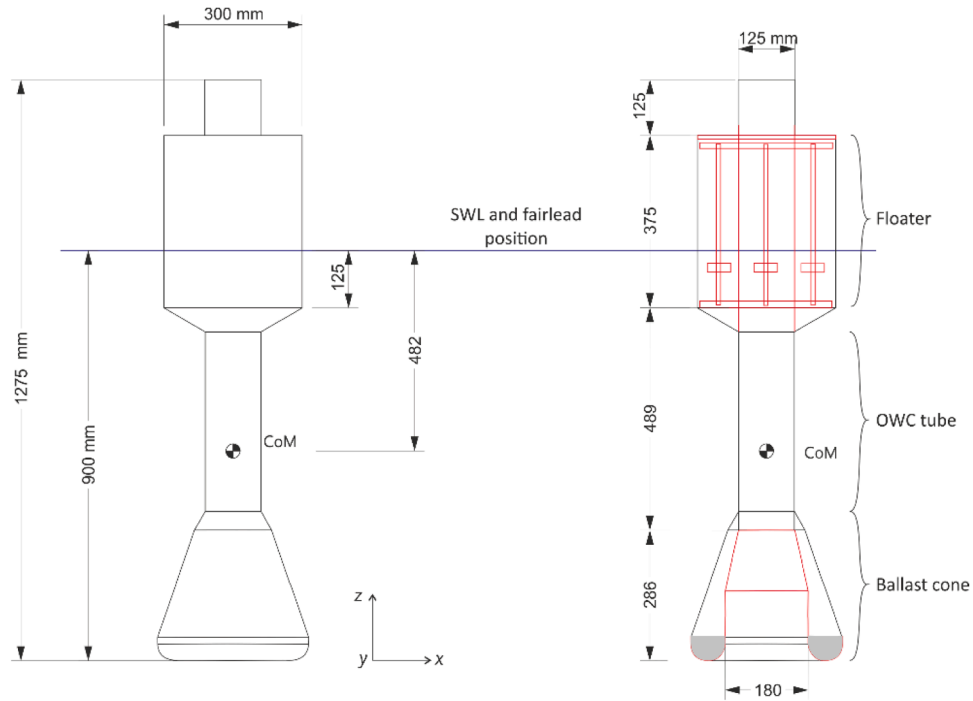


Fig. 1. The IST Spar-buoy model (a) Outer view (b) Inner cross-section .

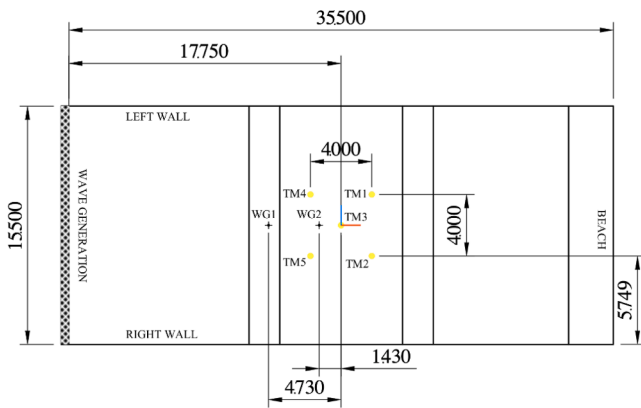


Fig. 2. Array layout within Ocean Basin and wave gauge location used during empty tank tests.

array to be investigated.

The interconnecting mooring lines were designed to match the static restoring force in surge provided by the independently-moored devices using intermediary clump weights. The mooring component arrangement is shown in Fig. 4, and properties are summarised in Table 1. It comprises mooring lines cut to length from Dyneema (UHMWPE - ultra-high molecular weight polyethylene) rope and connected to stainless steel chain sections (B_c), which were bolted to the basin floor to replicate the seabed anchor. The float mass was divided into cylindrical sections cut from closed-cell extruded polystyrene foam and the clump weights were cylindrical bar sections of lead. B_{clp} relates to the distance between the fairlead and the connection of the clump weight on the seabed line and B_l refers to the total length of Dyneema (Howey, 2020). The lengths of the Dyneema inter-body lines IBL1 and IBL2 are also given in Table 1.

A snapshot of the isolated device in the wave basin during experiments is shown in Fig. 5, with mooring components labelled. Further details on the mooring design for each configuration are given by the authors in an investigation of mooring loads and survivability of compact wave energy converter arrays (Gomes et al., 2020). The

mooring design was carried out using a quasi-static mooring line model considering inelastic and weightless lines and an inelastic catenary for the bottom mooring lines. The model was applied to determine the mooring line tensions and angles at the fairlead when a device was subjected to a specific displacement, therefore evaluating the mooring stiffness. In the particular case of the arrays with inter-body connections, the forced displacement of a device also introduced displacements in the interconnected devices, which required a momentum balance in all devices. The mooring design had the objective of minimizing the difference between the specified surge stiffness and those determined by the model while guaranteeing a force balance in all devices for the still water condition.

2.2. Spar-buoy model and instrumentation

The Spar-buoy models were designed to allow small adjustments of the centre of mass and moments of inertia using moveable ballast. The vertical location of the centre of mass (COM) and the inertial properties were measured using a swing test (Stratigaki et al., 2014). The results of these measurements are given in Table 2. Small differences were inevitable due to the construction tolerances and measurement accuracy for the centre of gravity and moment of inertia, and repeat measurements were made to quantify these differences (Howey, 2020). The maximum difference between devices was found to be 1% for the model mass, 2% for the vertical position of the centre of mass and 15% for the moment of inertia about a horizontal axis passing through the COM (I_{yy}).

A 19 mm diameter orifice plate was installed at the top of the OWC to act as a PTO. A differential pressure transducer measured the pressure difference across the orifice. Due to the large pitch motions previously observed when testing the IST Spar-buoy (Correia da Fonseca et al., 2016) it was decided not to install wave gauges inside the OWC to measure the motion of the water column. Instead the discharge coefficient (C_D) for each orifice plates was measured prior to testing using the driven piston technique described in Thiebaud et al., 2015. Volume flow (Q) was then calculated from the absolute value of the pressure difference (Δp) using the incompressible flow model:

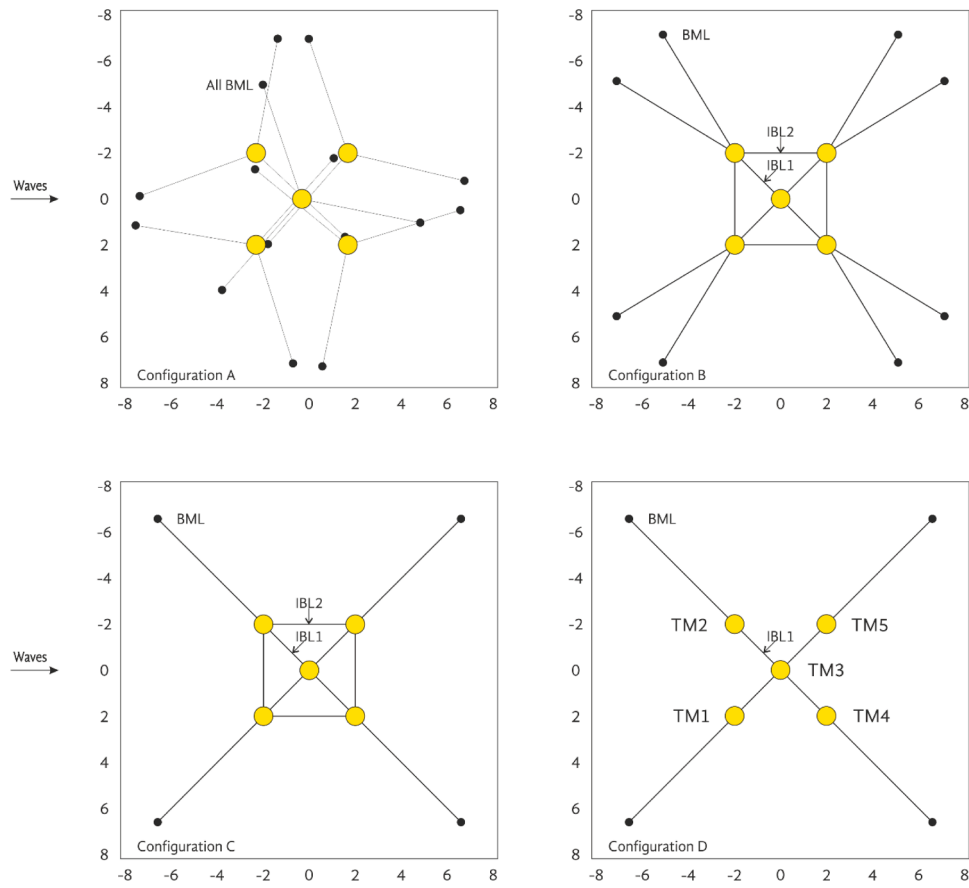


Fig. 3. Mooring Configurations A–D. Waves propagate from left to right. Device naming is indicated only on Configuration D, but is the same for all configurations. Placement of devices, anchors and mooring lines are drawn to scale, but the devices are enlarged for clarity.

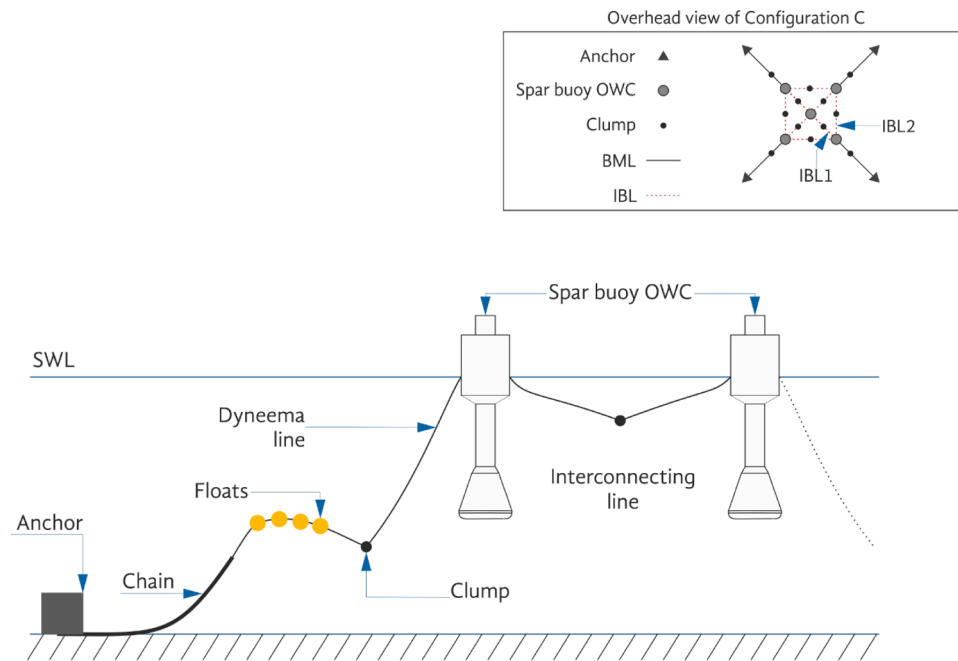


Fig. 4. Mooring Components with notation defined.

$$Q = AC_b \sqrt{\frac{2\Delta\rho}{\rho_a}}$$

(1)

where A is the cross-sectional area of the orifice and ρ_a is the density of air. Symmetrical flow conditions were assumed for inhalation and exhalation. The time averaged extracted power ($\overline{P_{dev}}$) was calculated by:

Table 1
Mooring line properties for each configuration, notation defined in Fig. 3.

Config.	Parameter		BML	IBL 1	IBL 2
A	Pre-tension at fairlead	[N]	16.0		
	B_1 rope length	[m]	5.01		
	B_{cl} Clump weight mass	[kg]	1.81		
	B_{clp} Clump weight position	[m]	1.29		
	B_f Floater mass	[g]	5		
	B_c chain length	[m]	1.16		
	B_{cd} chain diameter	[mm]	4		
B	Pre-tension at fairlead	[N]	5.8	6.4	3.4
	B_1 rope length	[m]	4.63	2.63	3.79
	B_{cl} Clump weight mass	[kg]	0.34	0.39	0.16
	B_{clp} Clump weight position	[m]	2.38	1.31	1.89
	B_f Floater mass	[g]	25		
	B_c chain length	[m]	1.93		
	B_{cd} chain diameter	[mm]	6		
C	Pre-tension at fairlead	[N]	11.3	6.2	3.4
	B_1 rope length	[m]	4.31	2.63	3.79
	B_{cl} Clump weight mass	[kg]	0.87	0.38	0.17
	B_{clp} Clump weight position	[m]	1.81	1.32	1.90
	B_f Floater mass	[g]	35		
	B_c chain length	[m]	2.68		
	B_{cd} chain diameter	[mm]	6		
D	Pre-tension at fairlead	[N]	11.7	11.5	
	B_1 rope length	[m]	3.59	2.67	
	B_{cl} Clump weight mass	[kg]	0.58	0.80	
	B_{clp} Clump weight position	[m]	2.13	1.33	
	B_f Floater mass	[g]	45		
	B_c chain length	[m]	3.40		
	B_{cd} chain diameter	[mm]	6		

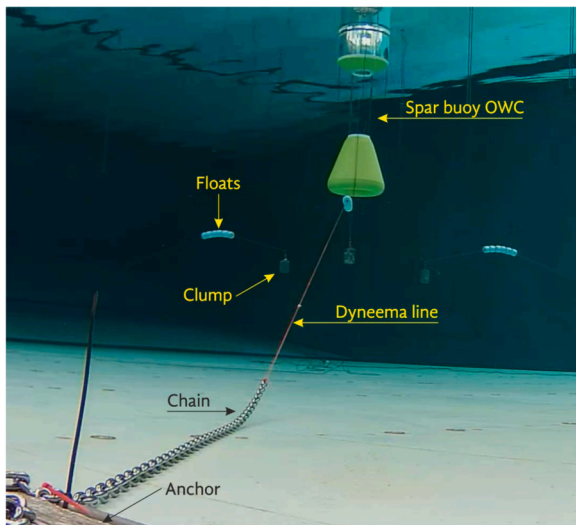


Fig. 5. Isolated spar-buoy device installed in the wave basin with components of different bottom mooring lines (BML) labelled. .

Table 2
Measured mass properties of each individual device.

Characteristic	TM1	TM2	TM3	TM4	TM5
Mass [kg]	18.73	18.77	18.92	18.83	18.74
CoM to MWL [mm]	481	475	470	476	475
I_{yy} [kg m ²]	3.40	3.40	3.92	3.69	3.69

$$\overline{P}_{dev} = \frac{1}{t_f - t_i} \int_{t_i}^{t_f} \Delta p Q dt \quad (2)$$

where t_i and t_f are the initial and final time of the analysis, which relate to the 25 wave periods after the wave field had stabilized.

An optical tracking system (Qualisys) was used to record the 6-

degree of freedom motions of each device. A global origin for the basin coordinate system was established at the centre of the basin. Each device was defined as a rigid body during calibration, and the origin of the local coordinate system was translated to the centre of gravity of the device. All motions (surge, sway, heave, roll, pitch and yaw) were then recorded relative to the global system. Regular wave motion response amplitude operators (RAOs) were calculated using the motion amplitudes and the wave amplitudes measured at WG1 before the devices were installed. Measurements were conducted with a minimum sampling frequency of 128 Hz.

2.3. Wave conditions

The influence of the different array configurations on performance was measured in both regular waves and irregular sea states. Regular wave tests were carried out at a constant wave height of $H = 0.05$ m and at frequencies between $f = 0.3$ Hz and $f = 1.0$ Hz for 180 s. A frequency interval of 0.05 Hz was used, with extra frequencies tested when resonances were identified. Three irregular sea states were tested with a significant wave height of $H_{mo} = 0.05625$ m and peak periods of $T_p = 1.2$ s, 1.57 s and 1.93 s for 600 s using a Pierson-Moskowitz spectrum, suited to sites exposed to fully-developed Atlantic sea-states. These were selected to represent frequently experienced sea states encountered at the test site chosen for this study off the coast of Leixões (Portugal), and is based on data generated from a MAR3G 3rd generation numerical model of a simulated ten year period, using ECMWF (European Centre for Medium-Range Weather Forecasts) wind fields as the input (Howey, 2020). The test site is located approximately 5–8 km off the coast of Leixões and has a water depth of 60–90 m.

3. Results

3.1. Decay tests

The heave natural frequency and damping of the central array device (TM3) and one outer device (TM2) were measured using decay tests in each array configuration. A pulley system was used to generate initial displacements and attempt to initiate heave-only motion. Each decay test was conducted three times, and this yielded a maximum difference in the natural frequency of 1% between repeats. Results are presented in Table 3.

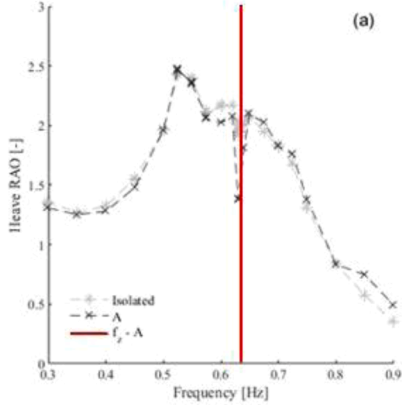
A difference of 0.02 Hz was observed in the heave natural frequency of the central array device (TM3) between Configuration A and Configuration I. The same test model and mooring arrangement were used for Configuration I and A tests, and so this effect is not caused by variations in the model as built. It is believed the difference may be due to hydrodynamic array interactions caused by radiated waves reflecting back from the surrounding devices in Configuration A and interacting with the central device. Hydrodynamic array interaction may also explain the difference between the natural frequency of TM3 and TM2 in Configuration A, which were both moored in the same way, although there is a relatively high standard deviation in decay test measurements

Table 3
Heave resonance frequency of central device (TM3) and an outer device (TM2) during decay tests.

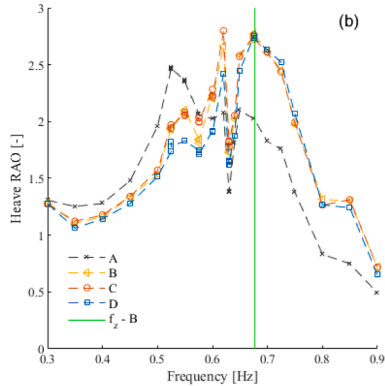
Configuration	Device	Mean Natural Frequency [Hz]	Standard Deviation
I	TM3	0.651	0.003
A	TM3	0.635	0.004
	TM2	0.619	0.013
B	TM3	0.677	0.001
	TM2	0.673	0.001
C	TM3	0.679	0.000
	TM2	0.686	0.003
D	TM3	0.680	0.002
	TM2	0.675	0.005

for TM2. The small differences in individual test model properties as-built (Table 2), small differences in mooring components, and the different location relative to basin walls of TM2 and TM3, may partly explain the differences in natural frequency observed, although the difference is not consistent across the array Configurations B-D.

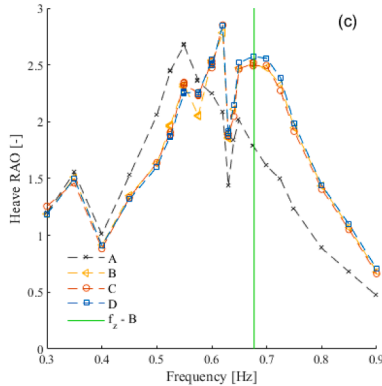
Using an interconnected mooring system (Configurations B, C and D) was found to increase the natural heave frequency for both the central and outer devices compared to the individually moored cases (Configuration A).



(a) The central device (TM3) in array Configuration A and when tested in isolation,



(b) The central device (TM3) in different array configurations



(c) The averaged outer devices in different array configurations.

Fig. 6. Heave RAOs. Vertical lines indicate natural frequencies measured during decay tests. (a) The central device (TM3) in array Configuration A and when tested in isolation, (b) The central device (TM3) in different array configurations (c) The averaged outer devices in different array configurations.

3.2. Heave in regular waves

Comparison between the heave responses of devices in different test configurations is shown in Fig. 6. In Fig. 6(a), the heave RAO of the central device in array Configuration A is compared with the device in isolation; in Fig. 6(b), the heave RAO of the central device in each of the four Configurations is plotted; and in Fig. 6(c), the heave RAO of the outer devices is compared for each of the four Configurations. The heave RAO for the outer devices in Fig. 6(c) is calculated as the mean of the RAO for TM2, TM4 and TM5.

Fig. 6(a) shows the heave RAO of an isolated device and the central device of Configuration A. Both were tested in the same location within the basin. The resonant frequency measured during the decay tests is indicated with a vertical red line ($f = 0.63$ Hz). However, at this frequency, a sharp reduction was observed in the heave response. This frequency corresponds to the 8th harmonic of the tank, and it is likely that the superposition of the incident wave and the generated standing wave across the tank results in a reduction in wave amplitude at the central device's location, thus reducing the heave response of the device.

The peak in heave response shown in Fig. 6(a) for both the isolated device and for Configuration A occurred at 0.525 Hz, significantly lower than the heave decay natural frequency. Previous studies of floating OWC type WECs, have shown double-peaked heave response (Gomes et al., 2015), with peaks corresponding to the device's heave resonant frequency and the resonant frequency of the water column. By assuming an effective length of zero, the resonant frequency of the water column for this device can be estimated as 0.53 Hz. It is therefore concluded that the main peak in heave is due to the water column resonance.

Only minor array effects were observed in the non-interconnected array for the majority of wave frequencies tested. When comparing the isolated device and the central device of Configuration A (Fig. 6(a)) at frequencies below $f = 0.8$ Hz (and neglecting responses at $f = 0.63$ Hz), the maximum difference was $\pm 5\%$. At frequencies above $f = 0.8$ Hz, the array effects become more significant, with a 30% increase in heave motion response of the central device in Configuration A.

In Fig. 6(b) and Fig. 6(c), the heave response of the central device and outer devices respectively for all four array configurations are compared, with noticeable differences observed between the individually moored cases (Configuration A) and the interconnected cases (Configurations B-D). At frequencies above 0.60 Hz, the interconnected array exhibited greater heave response than the individually moored array, with a peak occurring at 0.68 Hz, corresponding to the shift in the heave resonant frequency to this value, as measured during the decay tests and indicated by the vertical green line. At lower frequencies, the individually moored array had the greatest heave response, although all cases again had a peak associated with the resonance of the water column. An additional, and for the outer devices larger, peak in heave was observed at 0.62 Hz for the interconnected cases. This corresponds to the wavelength being approximately equal to the array spacing so that the outer devices were oscillating in phase with each other and in antiphase with the central device. The increased heave response, therefore may be due to a positive interconnection effect occurring.

Evidence for the formation of a standing wave is provided by comparing time series plots of the wave-only tests with those recorded during device experiments, plotted in Fig. 7. Constructive and destructive interference were both seen, depending on wave gauge location and the resulting phase relationship between the standing wave and incident wave. The difference between wave-only (empty tank) and wave plus device wave amplitude increases with time as the standing wave gains energy due to the resonance of the device and array being excited. The wave-only amplitude is constant between transients occurring as the wave maker signal starts and ends and then reduces to a value close to zero. With the array in place, reflections from the array interact with the basin side walls and cause a standing wave to be set up. This is because the wave frequency coincides with the cross-wave natural frequency of the basin, which matches the natural frequency of the device in heave

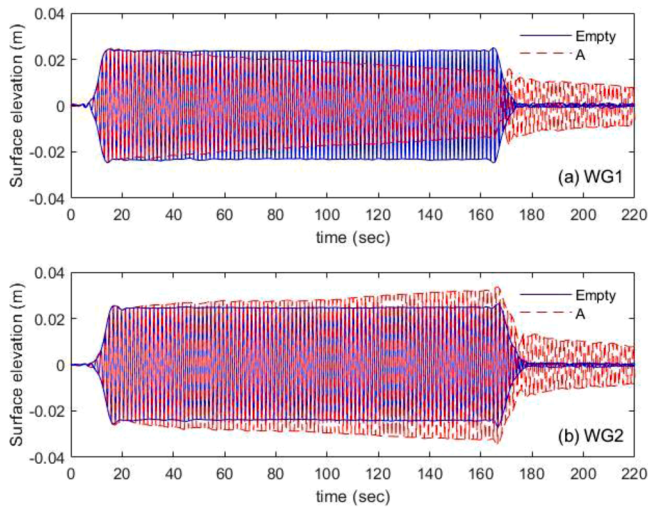


Fig. 7. Surface elevation measured at (a) WG1 and (b) WG2 during both empty tank (wave only) tests and array Configuration A tests with regular waves of $f = 0.63$ Hz.

indicated Fig. 6(a). In Fig. 7(a), the amplitude of the time series reduces in time due to destructive interference between the incident wave and the standing wave, and in Fig. 7(b), constructive interference is observed. Both wave gauges also measured a persistent oscillation that continues after the wave paddle has stopped at 180 s during the device experiments, further demonstrating the standing wave. This phenomenon has been confirmed with numerical modelling of the experiments both with and without the presence of tank walls (Howey, 2020), and the subsequent effects on the device performance at frequencies matching the harmonics of the tank has been quantified.

The array effects were quantified by calculating the ratio (q_{mA}) of the heave RAOs of the central device in the different tests (RAO_X) with the heave RAO of the central device of Configuration A (RAO_{TM3A}):

$$q_{mA} = \frac{RAO_X}{RAO_{TM3A}} \quad (3)$$

This is shown in Fig. 8.

From Fig. 8 it can be observed that the decrease in heave response at $f = 0.63$ Hz was greater for the central device when in an array than

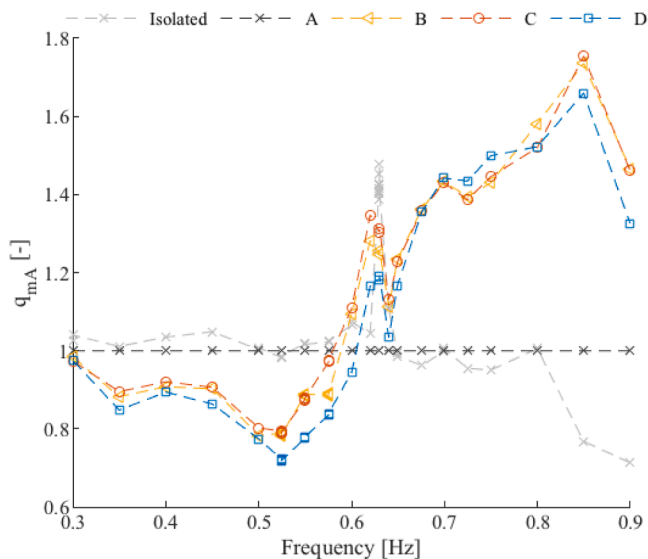


Fig. 8. The ratio (q_{mA}) of heave RAOs of the central device (TM3) of each configuration with respect to the central device of Configuration A.

when the device was isolated. The location of the outer four devices of the array approximately align with locations of antinodes of the generated standing wave. Their oscillations further increase the size of the standing wave, increasing the impact on heave.

3.3. Capture width ratio in regular waves

The capture width ratio was calculated to represent the hydrodynamic efficiency of the device normalised by the sum of the characteristic device widths in the array, using Eq. (4), where \bar{P}_{array} is the average array power output of an array of N devices, each of width W , and \bar{P}_{inc} is the incident wave power.

$$CWR = \frac{\bar{P}_{array}}{\bar{P}_{inc}WN} \quad (4)$$

Fig. 9 shows the capture width ratios for the different array configurations in regular waves. In Fig. 9(a), the CWR of the central device, TM3 is compared in each configuration, and in Fig. 9(b), the average CWR of all devices in the array is compared for each configuration (with the CWR for the device in the isolated configuration multiplied by five). In Fig. 9(a), similar performance characteristics can be observed for the isolated device and for the array of individually moored devices (TM3_I and TM3_A), although both the central device (TM3) and the overall array performance showed slight differences between Configurations I and A due to array affects. Whether these differences were positive or negative was frequency-dependent, and differences were not significant in comparison with the differences seen due to the effect of interconnecting the array. This is in agreement with the heave results as the heave motion dominated the water column motions and hence the power captured. For Configurations I and A, a peak in CWR occurred around 0.525 Hz, corresponding to the peak in heave observed due to the water column resonance. A second peak was observed around the heave resonance of the device, but with a significant reduction in performance at 0.63 Hz, matching the reduction in heave at this frequency.

There were only slight differences between the performance of the interconnected arrays (Configuration B-D). Configuration B demonstrates a drop in CWR compared with Configurations C and D at 0.575 Hz, and Configuration D demonstrated a slight increase in performance around 0.68 Hz. CWR peaked at 0.675 Hz for all three interconnected Configurations, in agreement with the heave resonance frequency measured from decay tests. The magnitude of capture width ratio at this frequency was 2.1 times the CWR at the largest peak for the individually moored array. A secondary peak was observed at 0.62 Hz, corresponding to the suspected positive interconnection effect occurring at this frequency.

The magnitude of heave of the interconnected devices at 0.675 Hz was similar to the magnitude of heave in the individually moored array at 0.55 Hz. However, the capture width ratio of the interconnected devices at 0.675 Hz was much larger than the capture width ratio of the individual devices at 0.55 Hz. The capture width ratio for the interconnected cases was also greater at the 0.68 Hz peak than at the 0.62 Hz peak, even though the heave at 0.62 Hz was greater. This phenomenon is due to the change in the phase relationship between the heave of the devices and the motion of the water column as frequency increased (Fig. 10). As frequency increased the phase angle tended to π , as also found by (Gomes et al., 2016). This is beneficial for energy extraction as the resultant air passing through the turbine is the volume of air associated with device heave displacement plus the displacement of the water column, and so increases in heave at higher frequencies, therefore result in greater increases in capture width ratio.

3.4. Performance in irregular sea states

The performance of each configuration in irregular sea states is shown in Fig. 11. It can be seen that the interconnected arrays

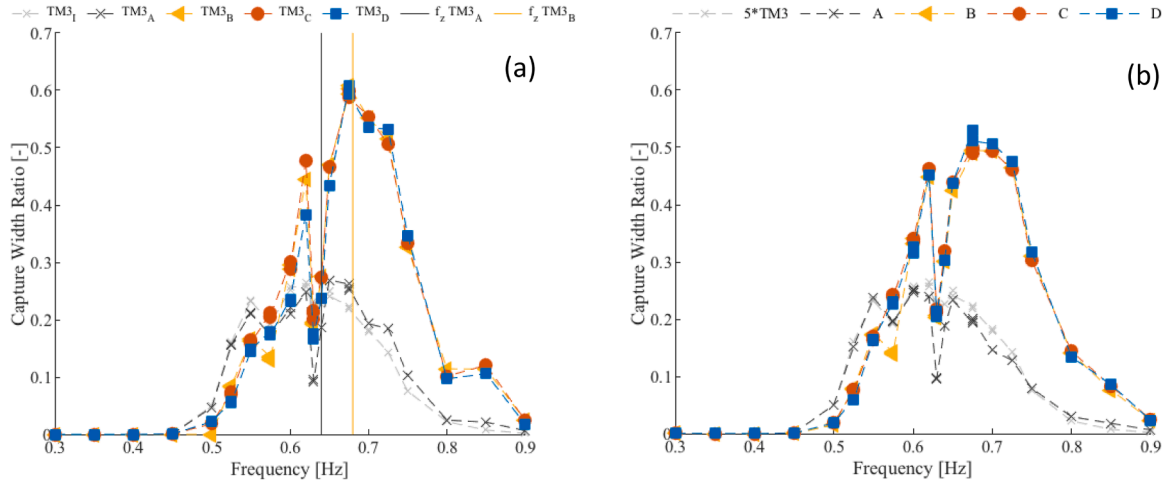


Fig. 9. Capture width ratio obtained with an incident wave amplitude of 0.025 m, (a) for the central device in all configurations with an isolated TM3I device in grey and (b) for all devices in each configuration with five times the isolated TM3I device in grey.

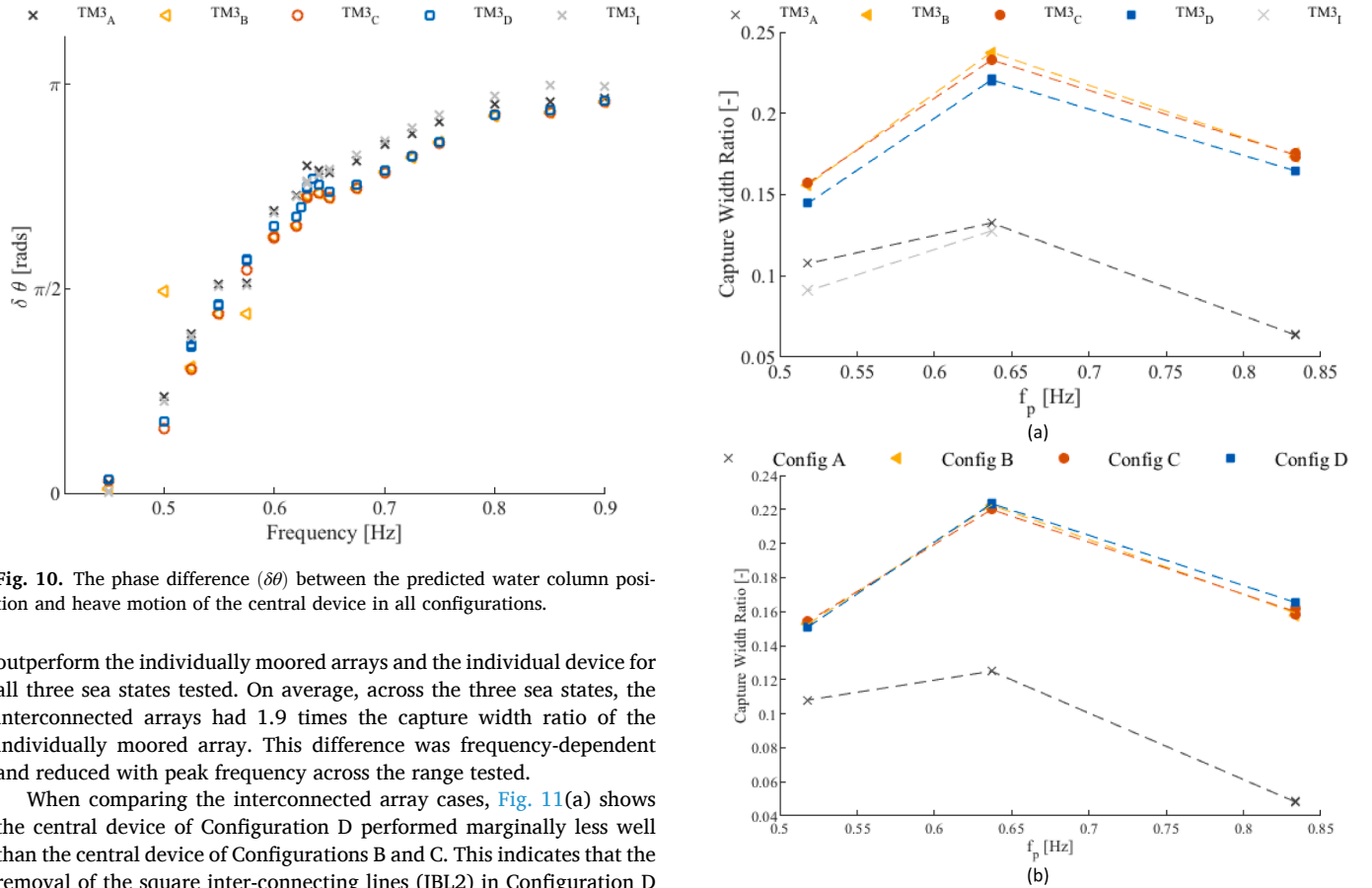


Fig. 10. The phase difference ($\delta\theta$) between the predicted water column position and heave motion of the central device in all configurations.

outperform the individually moored arrays and the individual device for all three sea states tested. On average, across the three sea states, the interconnected arrays had 1.9 times the capture width ratio of the individually moored array. This difference was frequency-dependent and reduced with peak frequency across the range tested.

When comparing the interconnected array cases, Fig. 11(a) shows the central device of Configuration D performed marginally less well than the central device of Configurations B and C. This indicates that the removal of the square inter-connecting lines (IBL2) in Configuration D reduced central device performance, although total array performance was marginally higher for two of the three sea states tested.

To quantify the effects of the array on the power capture, we computed the ratio between the power capture in an array and that captured by the individual device, also known as the q_o -factor, using Eq. (5):

$$q_o = \frac{\bar{P}}{\bar{P}_{ind}N} \quad (5)$$

Where \bar{P} is the array power, \bar{P}_{ind} is the power of an individual device, and N is the number of devices ($N = 1$ for an individual device and $N = 5$

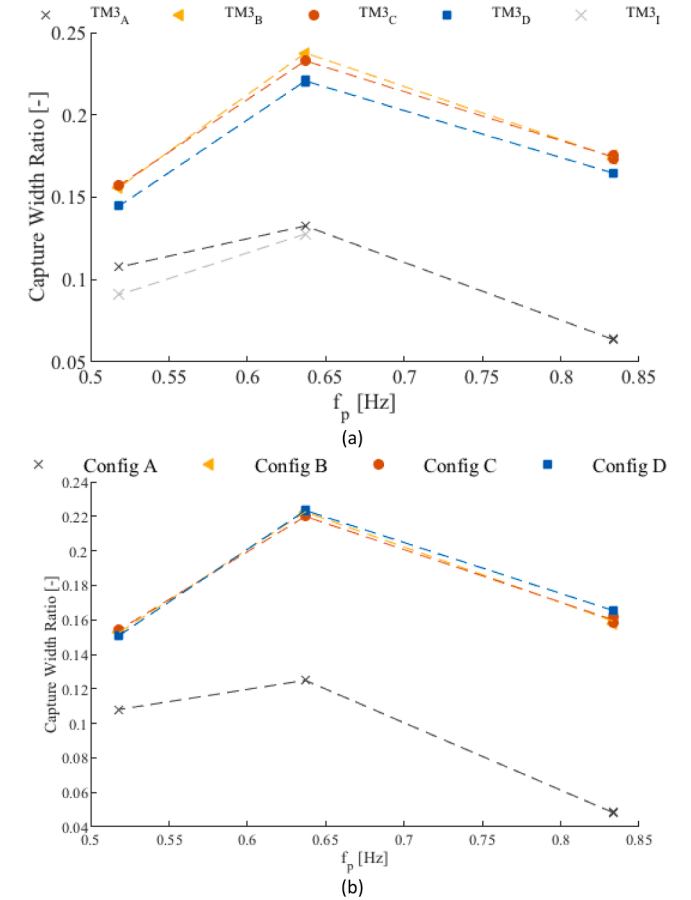


Fig. 11. Capture width ratios against peak frequency for (a) the central device in all configurations and (b) the total array output. $H_s = 0.05625$ m for all sea states.

for the whole array). The q_o -factors are given in Table 5: q_o -factors for interconnected moored array (Configuration B) by array rows and columns for irregular sea state with $f_p = 0.518$ Hz. for the individually moored array (Configuration A), and in Table 5 for Configuration B, for the $f_p = 0.518$ Hz case. The results for Configurations C and D were very similar to those of Configuration B and so are not presented in the same detail.

The individually moored array (Configuration A) had a total array q_o -

factor of 1.19 indicating that there was considerable constructive array interaction and this resulted in the individually moored case yielding a higher power output than five isolated devices. The overall q_o -factor suggests a 20% performance enhancement due to array interaction, which is consistent with Fig. 9. Furthermore, in Table 4, all Configuration A q_o -factors are greater than one, indicating that all the devices within the array out-performed the isolated device for this specific sea state.

The q_o -factors for the interconnected cases showed further performance enhancements, as was seen in the regular wave conditions; all interconnected q_o -factors were higher than those of the individually moored Configuration. The overall q_o -factor was 1.19 for the individually moored array and between 1.66 and 1.70 for Configurations B–D. This represents an increase of 39–43%, demonstrating the positive impact on performance resulting from interconnecting.

When considering intra-array differences, the trends were the same for the individually moored array and the interconnected arrays, although the magnitudes of the CWR were different. In all cases, the devices up-wave of the centre of the array outperformed the devices down-wave of the centre. There was a mean 13% reduction from the up-wave to the down-wave row for Configuration A, and 12.4% reduction for Configuration B. This is likely to be due to the shadowing effect of the down-wave devices in the array caused by those up-wave.

For both Configurations A and B, the two devices on the right-hand side of the array outperformed the two devices on the left. There was an average 12.5% increase in q_o -factor between the right and left-hand sides of the array for Configuration A and a 20.0% increase for Configuration B. The array was symmetrical in the basin. Slight asymmetries in mooring arrangement between the two sides of the array were introduced in Configuration A due to rotations in the 3-point mooring to fit the basin. However, this was not the case for Configuration B. It is possible that the slight construction differences in individual device models may be the cause, with the differences exaggerated by interconnecting the array. To understand whether these differences are due to model discrepancies, model variations, tank effects or natural variation, further scenarios would need to be investigated in future work, with systematic swapping of individual models between positions in the array.

3.5. Performance in irregular sea states – Annual yield

To compare the power performance of the different array configurations, the occurrence matrix and the regular capture width curves are used to predict the annual energy extraction at the Leixões test site using the methodology set out in (Babarit, 2015). The incident wave energy available to the array associated with each sea state of the occurrence matrix is calculated from the Pierson-Moskowitz spectrum, and the total energy available to the array *per annum* is the sum of the energy available across all possible sea states. The power output from the arrays was then calculated by multiplying the incident wave power by the capture widths and integrating with respect to frequency. The experimentally

Table 4

q_o -factors for individually moored array (Configuration A) by array rows parallel with and normal to the incoming wave direction for irregular sea state with $f_p = 0.518$ Hz.

	Up-wave	Centre	Down-wave	Parallel to incoming wave direction
Left	1.17 (TM1)		1.08 (TM4)	1.12
Centre		1.19 (TM3)		1.19
Right	1.34 (TM2)		1.19 (TM5)	1.26
Normal to incoming wave direction	1.25	1.19	1.13	Total mean = 1.19

Table 5

q_o -factors for interconnected moored array (Configuration B) by array rows and columns for irregular sea state with $f_p = 0.518$ Hz.

	Up-wave	Centre	Down-wave	Parallel to incoming wave direction
Left	1.68 (TM1)		1.47 (TM4)	1.57
Centre		1.71 (TM3)		1.71
Right	1.88 (TM2)		1.65 (TM5)	1.77
Normal to incoming wave direction	1.78	1.71	1.56	Total mean = 1.66

measured array average capture width ratio curves were first multiplied by the total width of the devices within the array and scaled to full scale. The power capture for an individual sea state (P_s) was estimated using Eq. (6)

$$P_s = \rho g \int_0^{\infty} S(f) C_g(f) CW(f) df \quad (6)$$

where S is the wave spectrum (here assumed to be Pierson-Moskowitz), C_g is group velocity and CW is the measured regular wave capture width. Equation (6) was calculated for all possible sea states within the occurrence matrix for all four array configurations, approximated as a sum between the frequency bounds of the experimental data (0.3 – 0.9 Hz).

To verify this approach, Eq. (6) was used to predict the power captured by the arrays during the irregular sea state experiments. These predictions are compared to the measured results in Table 6 and demonstrate reasonable agreement. Configuration A shows the greatest divergence, with the model over-predicting the case of $f_p = 0.833$ Hz by ~12% and under-predicting the $f_p = 0.637$ Hz and $f_p = 0.518$ Hz by 8% and 5% respectively. These differences are likely due to non-linearity in the response of the array to irregular sea states not accounted for by the linear prediction methods used. However, the approach was considered accurate enough to assess the impact of interconnecting on the annual performance of the array.

The predicted annual energy extraction for each array configuration is given in Fig. 12. The total annual extracted energy for each configuration was 1.4, 2.4, 2.5 and 2.5 GWh for Configurations A, B, C and D, respectively, indicating a clear difference between the individually moored and the interconnected cases. The interconnected cases extract much more energy overall, particularly in the higher frequency sea states, as expected due to the higher peaks seen in the regular wave capture width ratios. With regard to comparisons between the interconnected cases, results suggest that the level of interconnection would not significantly alter the energy extraction on an annual basis.

It should be noted that the scale effects are non-trivial (Falcão and Henriques, 2014; Folley et al., 2012), and while laboratory-scale trends might be expected to reflect full-scale trends in behaviour well, specific power predictions should be treated with caution. This is because the scale model experiments are designed using Froude scaling relationships, and these will not correctly reproduce the viscous effects (lower Reynolds number at model scale) or the spring-like air compressibility

Table 6

Ratio of predicted array power in an irregular sea state using regular wave results and power measured directly during irregular sea state experiments for array Configurations A–D.

	Configuration			
f_p [Hz]	A	B	C	D
0.833	1.12	0.98	0.99	0.99
0.637	0.92	0.97	1.02	1.00
0.518	0.95	0.99	1.03	1.04

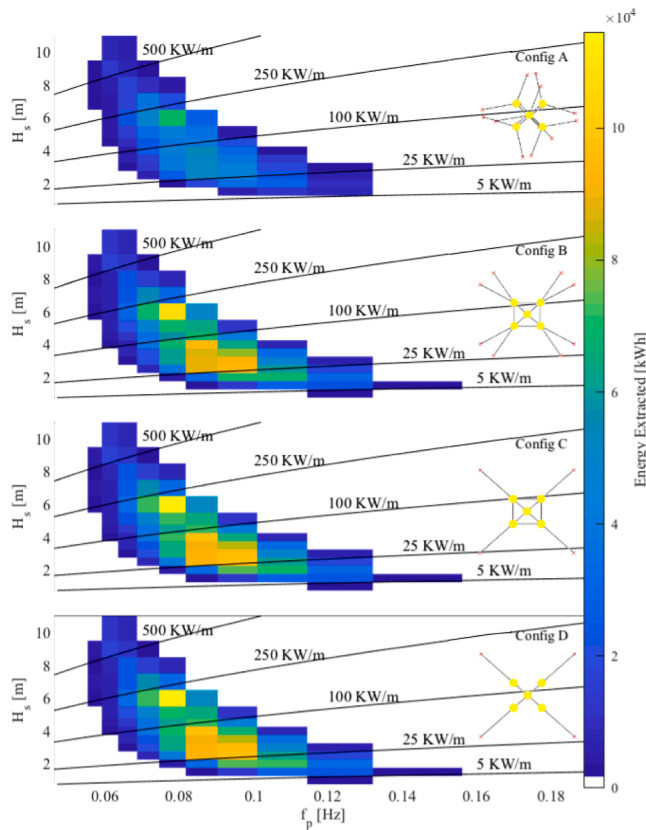


Fig. 12. Energy extraction matrix for all configurations using the probability matrix of a site of the coast of Leixões, Portugal.

effect in the OWC chamber.

4. Conclusions

This study examined the impact of interconnecting wave energy devices within an array on the overall power performance of the array. It has been shown that for the Spar-buoy OWC that significant improvements in performance can be achieved, with an increase in annual energy extraction predicted for a case study at Leixões, Portugal, of 75% from 1.4 GWh for the individually moored array to 2.5 GWh when devices within the array were interconnected. The level of interconnectivity and the number of mooring lines was systematically altered, and the performance enhancement above that for an individually moored array was found to be consistent for all interconnected arrays.

The results show a significant increase in performance and hence the potential to reduce the LCOE of WEC arrays, although this cannot be fully quantified without taking into account mooring loads. By interconnecting Spar-buoy devices, the heave resonance frequency was raised to a value at which the phase relationship between the device's heave and water column motion was favourable. There is also evidence that a positive intra-array effect occurred when the wavelength was equal to the array width for interconnected cases.

In addition to the power capture performance, the motions and loads experienced by the mooring system are affected by interconnecting the devices in the array. In this work, the mooring systems for each interconnected array was designed to achieve a balance of forces similar to the individually moored device in still water. However, when considering the loads experienced by each configuration under extreme conditions Gomes et al., 2020, the individually moored array of devices was found to experience the lowest mooring loads, and the inter-body mooring lines used in interconnected arrays frequently experienced

costly snap loading. It is recommended that, in order to benefit from the enhanced power capture available from using interconnected arrays, the inter-body lines should be carefully designed with sufficient length to accommodate the resulting motions without snap loads.

The increases in performance identified during this study are device-specific. The hydrodynamics of interconnected arrays is very complex, and there are many aspects that have not been covered here, such as variations in array orientation, spacing, size, individual mooring components and others. However, the results clearly indicate that the interconnecting of WECs within arrays may have a significant positive impact on performance. The influence that interconnecting has on device response also indicates that such an approach needs to be considered early in the design process.

The eventual adoption of array interconnection will depend not only on changes in performance but on the overall economics of a project. For example, interconnecting the devices reduces the number of anchors and mooring lines needed, but increases the load that these will experience. The addition of interconnecting lines may also result in more costly installation procedures and risks, reducing maintenance access to devices within the array. The reduction in array redundancy and the increased risk of cascade failure would also need to be considered when designing such a system. Nevertheless, the results presented here show strong promise for the enhancement of wave energy capture performance and array-level tuning through the interconnection of floating WEC arrays.

Declaration of Competing Interest

The authors declare that they have no known competing financial interests or personal relationships that could have appeared to influence the work reported in this paper.

Acknowledgments

This work was funded by EU Horizon 2020 under grant agreement No 641334: WETFEET - Wave Energy Transition to Future by Evolution of Engineering and Technology. This work was also partly supported by the Portuguese Foundation for Science and Technology (FCT) through IDMEC, under LAETA, project UIDB/50022/2020, and partly supported by the UKRI Supergen ORE Hub, EP/S000747/1.

References

- Ashton, I.G.C., Johanning, L., Linfoot, B., 2009. Measurement of the effect of power absorption in the lee of a wave energy converter. In: 28th International Conference on Ocean, Offshore and Arctic Engineering. American Society of Mechanical Engineers.
- Babarit, A., 2015. A database of capture width ratio of wave energy converters. *Renew. Energy* 80, 610–628.
- Brown, C., Poudineh, R., Foley, B., 2015. Achieving a cost-competitive offshore wind power industry: what is the most effective policy framework?, in *The Oxford Institute for Energy Studies Paper*. OIES PAPER: EL 15.
- Chang, G., Jones, C.A., Roberts, J.D., Neary, V.S., 2018. A comprehensive evaluation of factors affecting the levelized cost of. *Renew. Energy* 127, 344–354.
- Collins, K.M., Stripling, S., Simmonds, D.J., Greaves, D.M., 2018. Quantitative metrics for evaluation of wave fields in basins. *Ocean Eng.* 169, 300–314. <https://doi.org/10.1016/j.oceaneng.2018.09.010>.
- Correia da Fonseca, F.X., Gomes, R.P.F., Henriques, J.C.C., Gato, L.M.C., Falcão, A.F.O., 2016. Model testing of an oscillating water column spar-buoy wave energy converter isolated and in array: motions and mooring forces. *Energy* 112 (1), 1207–1218.
- Falcão, A.F.O., Henriques, J.C.C., 2014. Model-prototype similarity of oscillating-water-column wave energy converters. *Int. J. Marine Energy* 6, 18–34.
- Folley, M., Babarit, A., Child, B., Forehand, D., O'Boyle, L., Silverthorne, K., Spinneken, J., Stratigaki, V., Troch, P., 2012. A review of numerical modelling of wave energy converter arrays. In: *ASME 2012 International Conference on Ocean, Offshore and Arctic Engineering (OMAE2012)*, Rio de Janeiro, Brazil.
- Folley, M., 2016. Numerical Modelling of Wave Energy Converters - State of the Art Techniques For Single Devices and Arrays. Elsevier, London, UK.
- Gomes, R.P.F., Henriques, J.C.C., Gato, L.M.C., Falcão, A.F.O., 2012. Hydrodynamic optimization of an axisymmetric floating oscillating water column for wave energy conversion. *Renew. Energy* 44, 328–339.
- Gomes, R.P.F., Henriques, J.C.C., Gato, L.M.C., Falcão, A.F.O., 2015. Wave channel tests of a slack-moored floating oscillating water column in regular waves. In: *Proceedings*

- of the 11th European Wave and Tidal Energy Conference. Ecole Centrale de Nantes, France.
- Gomes, R.P.F., Henriques, J.C.C., Gato, L.M.C., Falcão, A.F.O., 2016. Wave power extraction of a heaving floating oscillating water column in a wave channel. *Renew. Energy* 99, 1262–1275.
- Gomes, R.P.F., Gato, L.M.C., Henriques, J.C.C., Portillo, J.C.C., Howey, B.D., Collins, K.M., Hann, M.R., Greaves, D.M., 2020. Compact floating wave energy converters arrays: mooring loads and survivability through scale physical modelling. *Appl. Energy* 280, 115982. <https://doi.org/10.1016/j.apenergy.2020.115982>. Volume.
- Gunn, K., Stock-Williams, C., 2012. Quantifying the global wave power. *Renew. Energy* 44, 296–304.
- Howey, B., 2020. A Physical and Numerical Study of an Interconnected Wave Energy Array, PhD Thesis. University of Plymouth.
- International Energy Agency. <https://www.iea.org> [Accessed on 20/05/2020].
- Jenne, D.S., Yu, Y.-H., Neary, V.S., Yu, Y.-H., 2015. Levelized cost of energy analysis of marine and hydrokinetic reference models. 3rd Marine Energy Technol. Symp. Washington, DC.
- Jin, S., Greaves, D.M., 2021. Wave energy in the UK: status review and future perspectives. *Renew. Sustain. Energy Rev.* 143, 110932. Volume.
- Krivtsov, V., Linfoot, B., 2014. Basin Testing of Wave Energy Converters in Trondheim: investigation of Mooring Loads and Implications for Wider Research. *J. Mar. Sci. Eng.* 2 (2), 326–335.
- O'Boyle, L., Elsässer, B., Whittaker, T., 2017. Experimental Measurement of Wave Field Variations around Wave Energy Converter Arrays. *Sustainability* 9 (1), 1–16.
- Reikard, G., Robertson, B., Bidlot, J.-R., 2015. Combining wave energy with wind and solar: short-term forecasting. *Renew. Energy* 81, 442–456.
- Ruiz, P.M., Ferri, F., Kofoed, J.P., 2017. Experimental Validation of a Wave Energy Converter Array Hydrodynamics Tool. *Sustainability* 9 (1), 115.
- Stratigaki, V., Troch, P., Stallard, T., Forehand, D., Kofoed, J.P., Folley, M., Benoit, M., Babarit, A., Kirkegaard, J., 2014. Wave basin experiments with large wave energy converter arrays to study interactions between the converters and effects on other users in the sea and the coastal area. *Energies* 7 (2), 701–734.
- Thiebaud, F., Pascal, R.C.R., Andreu, A.G., 2015. Investigation into the calibration of orifices used in OWC tank testing. In: Proceedings of the 11th European Wave and Tidal Energy Conference. EWTEC, Ecole Centrale de Nantes, France.
- Thomsen, J.B., Ferri, F., Kofoed, J.P., Black, K., 2018. Cost optimization of mooring solutions for large floating wave energy converters. *Energies* 11 (1), 1–23.
- Vicente, P.C., Falcão, A.F.O., Gato, L.M.C., Justino, P.A.P., 2009. Dynamics of arrays of floating point-absorber wave energy converters with inter-body and bottom slack-mooring connections. *Appl. Ocean Res.* 31 (4), 267–281.
- Weller, S.D., Stallard, T.J., Stansby, P.K., 2010. Experimental measurements of irregular wave interaction factors in closely spaced arrays. *IET Renew. Power Gener.* 4 (6), 628–637.
- Wiser, R.H., Jenni, K., Seel, J., Baker, E., Hand, M.M., Lantz, E., Smith, A., 2016. Forecasting Wind Energy Costs and Cost Drivers: the Views of the World's Leading Experts. IEA Wind Task 26. LBNL-1005717.
- Yang, S.-H., Ringsberg, J., Johnson, E., 2018. Analysis of interaction effects between WECs in four types of wave farms. In: Advances in Renewable Energies Offshore: Proceedings of the 3rd International Conference on Renewable Energies (RENEW 2018). Lisbon, Portugal. Lisbon, Portugal.